Ceramics International 50 (2024) 26929–26937

Contents lists available at ScienceDirect

Ceramics International

journal homepage: www.elsevier.com/locate/ceramint

High performance of $SrCo_{1-x}Zr_xO_{3-\delta}$ perovskite cathodes for IT-SOFCs

Mónica Chivite-Lacaba [a,b], Jesús Prado-Gonjal [a], José Antonio Alonso [b], María Teresa Fernández-Díaz [c], Vanessa Cascos [a,b,*]

[a] Dpto Química Inorgánica, Universidad Complutense de Madrid, Ciudad Universitaria s/n, Madrid, 28040, Spain
[b] Instituto de Ciencia de Materiales de Madrid, CSIC, Cantoblanco, 28049, Madrid, Spain
[c] Institut Laue Langevin, BP 156X, Grenoble, F-38042, France

ARTICLE INFO

Handling Editor: Dr P. Vincenzini

Keywords:
IT-SOFC
MIECs
Cathode materials
Neutron diffraction

ABSTRACT

Stabilization of a tetragonal perovskite structure in the $SrCoO_{3-\delta}$ system at room temperature has been achieved through wet chemical techniques, and it has been successfully tested in Solid Oxide Fuel Cells (SOFCs). Chemical substitutions at the Co position were carried out by introducing different amounts of zirconium ($SrCo_{1-x}Zr_xO_{3-\delta}$; $x = 0.05$, 0.08 and 0.11) to destabilize the columns of CoO_6 octahedra sharing faces in the competitive 2H-hexagonal phase. The crystal structure was studied by X-ray diffraction (XRD) and neutron powder diffraction (NPD) at 25 °C and correlated with mechanical and electrical properties. Chemical compatibility studies between the samples and the $La_{0.8}Sr_{0.2}Ga_{0.83}Mg_{0.17}O_{3-\delta}$ (LSGM) electrolyte revealed not interaction at high temperatures. Dilatometric analysis measurements showed a compatible thermal expansion with the LSGM electrolyte over the entire temperature range, demonstrating good mechanical compatibility. Furthermore, the relatively high conductivity values (~83 S cm^{-1} at 850 °C) indicated their suitability as cathodes in SOFCs. Finally, test cells prepared with an electrolyte (LSGM) supported configuration provided a maximum output power exceeding 600 mW/cm^2 using pure H_2 as fuel at 850 °C. Importantly, the performance of the cathode materials did not degrade after extended operation at this temperature.

1. Introduction

The constrained accessibility of fossil fuel reservoirs and the subsequent environmental and climatic repercussions emphasize the critical necessity of actively pursuing the development and implementation of alternative, sustainable energy sources [1,2]. This urgency is based on the recognition of the finite nature of fossil fuel reserves and the escalating adverse effects they have on the environment and climate. As we confront the challenges associated with resource depletion and the exacerbation of climate change, there is a heightened call for innovative and eco-friendly energy solutions to mitigate these concerns. This necessity highlights the pivotal role of transitioning towards alternative energy sources that not only address the limitations of fossil fuels but also contribute to a more resilient, cleaner, and environmentally responsible energy paradigm [3,4].

In this landscape, hydrogen is a versatile and clean fuel that, when used in fuel cells, undergoes electrochemical reactions to produce electricity, emitting only water vapour as a by-product. The increasing recognition of hydrogen as a sustainable energy carrier has positioned it as a central element in the drive towards cleaner and more environmentally friendly fuel alternatives [5].

Solid Oxide Fuel Cells (SOFCs) are electrochemical devices that directly convert the chemical energy of hydrogen into electrical energy through oxidation and reduction reactions occurring at the electrodes [6]. High operating temperatures, typically above 900 °C, have been a significant drawback for widespread adoption of SOFCs due to issues such as material degradation, thermal cycling stresses, and high manufacturing costs [7,8]. For this reason, the reduction of the operating temperature of SOFCs is considered a key challenge for their commercialization, and researchers have been exploring various strategies to achieve this goal [9].

The reduction of the working temperature poses challenges to the electrochemical reaction kinetics occurring at the interface between the electrode and electrolyte, leading to a decline in cell performance. The drawback of using pure electronically conductive materials is that the reaction occurs only at specific points, namely the triple phase boundary. To enhance the active area at the electrode-electrolyte interface, researchers are focusing on the development of mixed ionic and

* Corresponding author. Dpto Química Inorgánica, Universidad Complutense de Madrid, Ciudad Universitaria, s/n, Madrid, 28040, Spain.
E-mail address: vcascos@ucm.es (V. Cascos).

https://doi.org/10.1016/j.ceramint.2024.04.424
Received 30 January 2024; Received in revised form 16 April 2024; Accepted 30 April 2024
Available online 1 May 2024

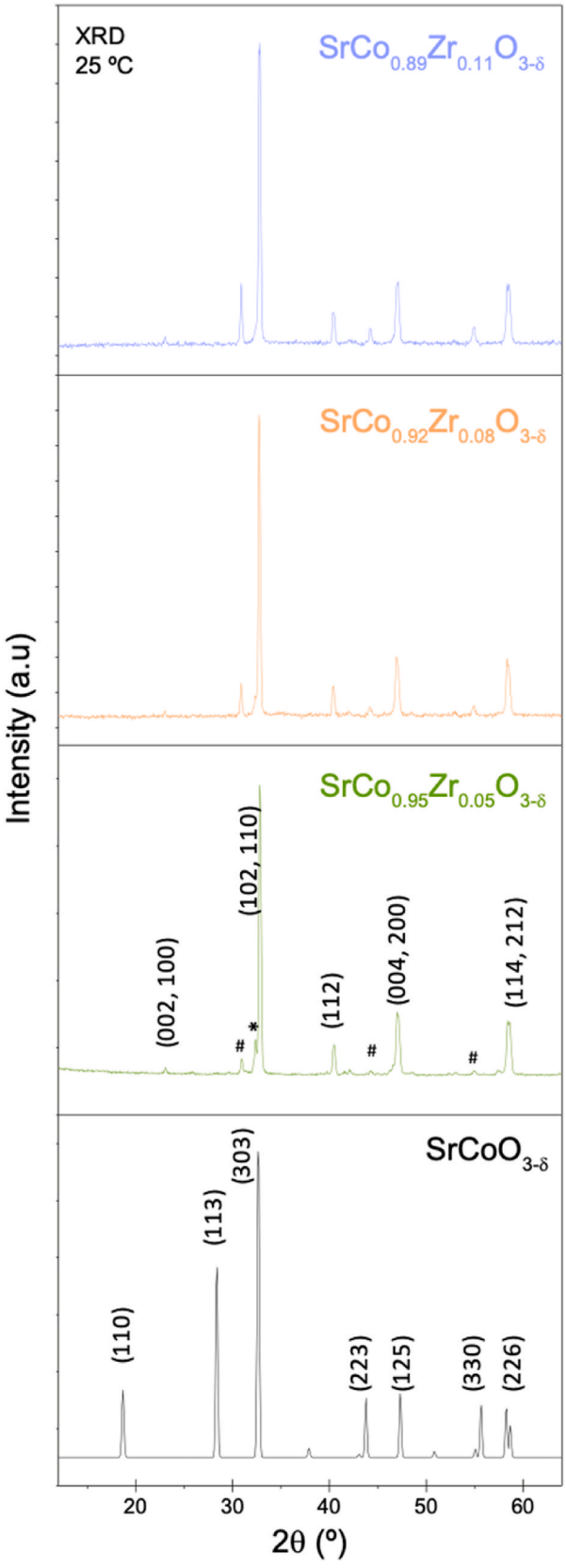

Fig. 1. XRD patterns collected with Cu Kα radiation for $SrCo_{1-x}Zr_xO_{3-\delta}$ (x = 0.05, 0.08 and 0.11) samples at 25 °C. The pattern at the bottom corresponds to the unwanted hexagonal phase, obtained with no Zr doping. The asterisk (*) shows the main reflection of the orthorhombic phase $Sr_2Co_2O_5$ while the hashtag (#) represents the main reflections of the cubic impurity $SrZrO_3$.

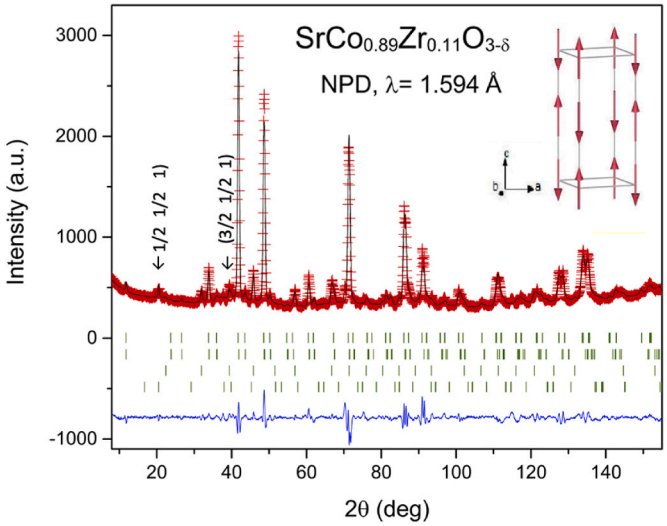

Fig. 2. Observed (red crosses), calculated (black solid line), and their difference (blue line) NPD profiles for $SrCo_{0.89}Zr_{0.11}O_{3-\delta}$ at RT. The series of Bragg reflections (green lines) correspond to the two coexistent perovskite phases as well as the impurity $SrZrO_3$ and the magnetic phase. The inset shows the G-type magnetic structure. (For interpretation of the references to colour in this figure legend, the reader is referred to the Web version of this article.)

electronic conductors (MIECs). The majority of MIECs fall under the category of perovskite-type oxides (type ABO_3), which are mixed metal oxides. These materials exhibit a broad range of oxygen stoichiometries and interesting transport properties due to the partial or complete substitution of elements in both the A and B sites of the perovskite structure. Among these, Co-based materials, especially those derived from $SrCoO_3$, have garnered considerable research attention due to their favourable electrochemical characteristics [10,11]. Notably, the high-temperature phase of $SrCoO_{3-\delta}$ has been recognized for displaying mixed conductivity, featuring significant values of oxygen permeability and electrical conductivity [12–14]. Nevertheless, the specific polymorphs exhibited by $SrCoO_{3-\delta}$ oxides at room temperature and normal pressure can vary based on the synthesis conditions. When samples are quenched from the reaction temperature, a brownmillerite-type orthorhombic structure is obtained. In this metastable phase, oxygen vacancies are ordered at long distances in layers of isolated zigzag chains of MO_4 tetrahedra, alternating with octahedral layers. On the other hand, when samples are slowly cooled from the reaction temperature, a hexagonal polymorph is obtained. While the brownmillerite structure exhibits excellent ionic and electronic transport properties, the hexagonal phase, containing face-sharing octahedra, shows extremely poor transport behavior. Unfortunately, the brownmillerite phase transitions to the hexagonal phase upon heating above 650 °C, making it unsuitable for direct use as a cathode in SOFCs. To address this challenge, stabilization of the '3C' perovskite-like structure, where polyhedra share vertices, has been used to develop an ionic-electronic mixed conductor under air conditions at intermediate temperatures. To achieve mixed ionic-electronic conductivity at moderate temperatures, scientists have leveraged the stability of the perovskite structure in either a tetragonal or cubic phase [15]. This involves introducing doping agents into the cobalt position, characterized by highly charged cations with elevated oxidation states, such as Sb^{5+}, Ta^{5+}, Nb^{5+}, Ti^{4+}, Ir^{4+}, Ru^{4+} [16–21]. The presence of these cations induces repulsive forces, disrupting the alignment of octahedral chains sharing faces and promoting the formation of a stable tetragonal or cubic structure. This structure, composed of layers of octahedra connected by shared vertices, remains stable throughout the entire operational temperature range of a SOFC [22,23].

In this work, the same strategy has been followed using zirconium as doping cation. $SrCo_{1-x}Zr_xO_{3-\delta}$ oxides (x = 0.05, 0.08 and 0.11) were

Table 1
Refined structural parameters of $SrCo_{0.89}Zr_{0.11}O_{3-\delta}$ consisting of two perovskite phases at room temperature from NPD data. Space group: P4/mmm. [a]Anisotropic Betas × 10^4. $b_{12} = b_{23} = b_{13} = 0$. *The remaining phase abundance percentage corresponds to the $SrZrO_3$ impurity, accounting for 11.90%.

Nominal Composition	$SrCo_{0.89}Zr_{0.11}O_{3-\delta}$	
Refined Compositions	$SrCo_{0.92}Zr_{0.08}O_{2.76}$	$SrCo_{0.97}Zr_{0.03}O_{2.76}$
Phase abundance (%)	46.70*	41.40*
Sr (1/2,1/2,*z*)		
a (Å)	*3.8712 (1)*	*3.8534 (1)*
c (Å)	*7.7588 (6)*	*7.7286 (7)*
V(Å^3)	*116.27 (1)*	*114.76 (1)*
Sr (1/2,1/2,*z*)		
z	*0.26188(1)*	*0.26188(1)*
B_{iso} (Å^2)	*1.05 (5)*	*1.05 (5)*
F_{occ}	*1.00*	*1.00*
Co1 (0,0,0)		
B_{iso} (Å^2)	*0.01 (1)*	*0.01 (1)*
F_{occ}	*1.00*	*1.00*
Moment (μ_B) Co1	*0.97(2)*	
(Co/Zr)2 (0,0,1/2)		
B_{iso} (Å^2)	*2.6(2)*	*2.6(2)*
F_{occ} Co/Zr	*0.421/0.079*	*0.469/0.031*
Moment (μ_B) Co2	*−0.97(2)*	
O1 (1/2,0,0)		
B_{iso}(Å^2)	*0.84(6)*	*0.84(6)*
F_{occ}	*1.00*	*1.00*
O2 (0,0,*z*)		
β^a_{11}	*629(52)*	*629(52)*
β^a_{22}	*629(52)*	*629(52)*
β^a_{33}	*23(7)*	*23(7)*
B_{eq} (Å^2)	*2.7058*	*2.6812*
z	*0.7710(7)*	*0.7710(7)*
F_{occ}	*0.980(2)*	*0.980(2)*
O3 (1/2,0,1/2)		
β^a_{11}	*385(60)*	*385(60)*
β^a_{22}	*344(78)*	*344(78)*
β^a_{33}	*404(33)*	*404(33)*
B_{eq} (Å^2)	*4.7089*	*4.6703*
F_{occ}	*0.782(1)*	*0.782(1)*
Reliability factors		
χ^2	*4.37*	*4.37*
R_p (%)	*2.72*	*2.72*
R_{wp} (%)	*3.74*	*3.74*
R_{exp} (%)	*1.79*	*1.79*
R_{Bragg} (%)	*5.71*	*5.97*
Distances (Å)		
Co1 – O1 (x4)	*1.93561(8)*	
Co1 – O2 (x2)	*1.776(5)*	
(Co,Zr)2 – O2 (x2)	*2.103(5)*	
(Co,Zr)2 – O3 (x4)	*1.93561(8)*	

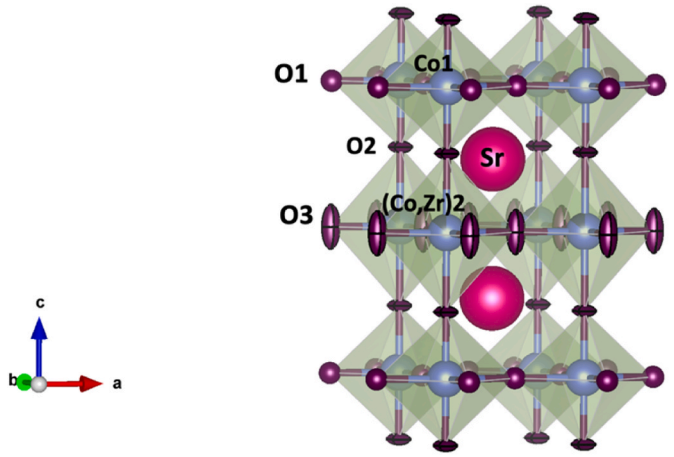

Fig. 3. *Tetragonal superstructure observed for* $SrCo_{0.89}Zr_{0.11}O_{3-\delta}$ *from NPD data at RT.*

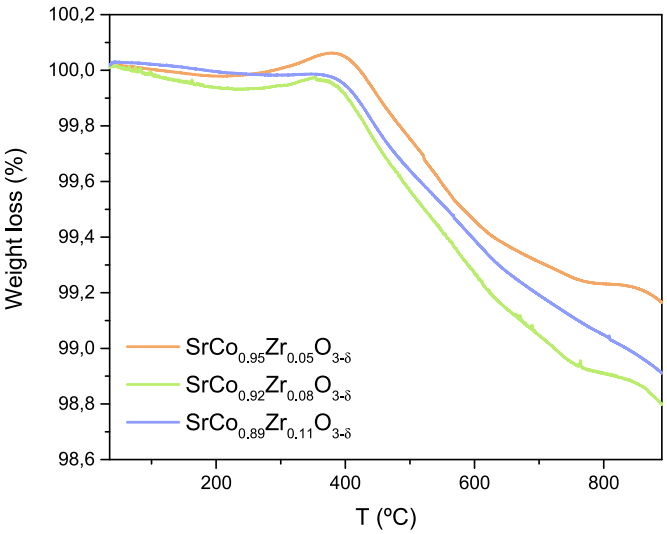

Fig. 4. TGA curves for $SrCo_{1-x}Zr_xO_{3-\delta}$ (x = 0.05, 0.08 and 0.11) perovskite in air flux.

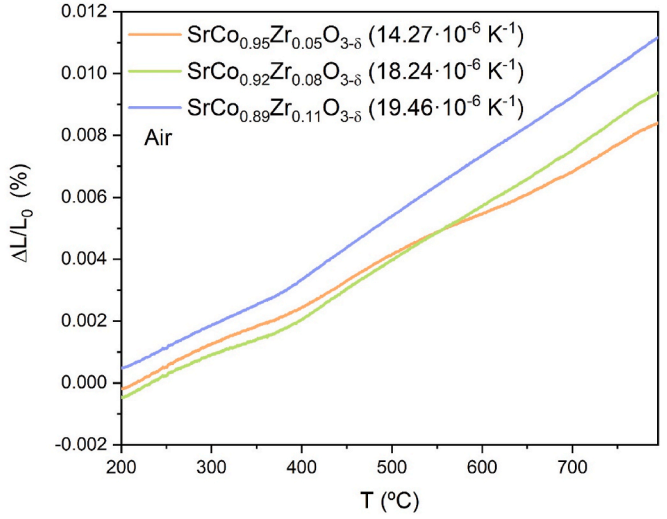

Fig. 5. Thermal expansion determined by dilatometry for $SrCo_{1-x}Zr_xO_{3-\delta}$ (x = 0.05, 0.08 and 0.11).

synthesized via a soft-chemistry approach through the incorporation of a small proportion of Zr^{4+} into the Co positions within the $SrCoO_{3-\delta}$ system. The stabilization process resulted in tetragonal *P4/mmm* perovskite superstructures, and these materials exhibited promising performance when used as cathodes in individual SOFCs. The crystal structure of $SrCo_{1-x}Zr_xO_{3-\delta}$ oxides (x = 0.05, 0.08 and 0.11) was analysed using X-ray diffraction (XRD) and neutron powder diffraction (NPD) techniques. The study delves into oxygen deficiency, electrical conductivity, ionic transport, and thermal expansion. Additionally, the electrochemical response of the ceramic materials was investigated through electrochemical impedance spectroscopy (EIS) analysis. In practical applications, the synthesized cathodes exhibit remarkable power density values when tested in single fuel-cell experiments, particularly when utilizing hydrogen as a fuel. This positions them as promising candidates for use as cathodes in SOFCs.

2. Experimental

$SrCo_{1-x}Zr_xO_{3-\delta}$ (x = 0.05, 0.08 and 0.11) perovskites were synthesized by the citrate method, a wet-chemistry technique. Metal nitrates,

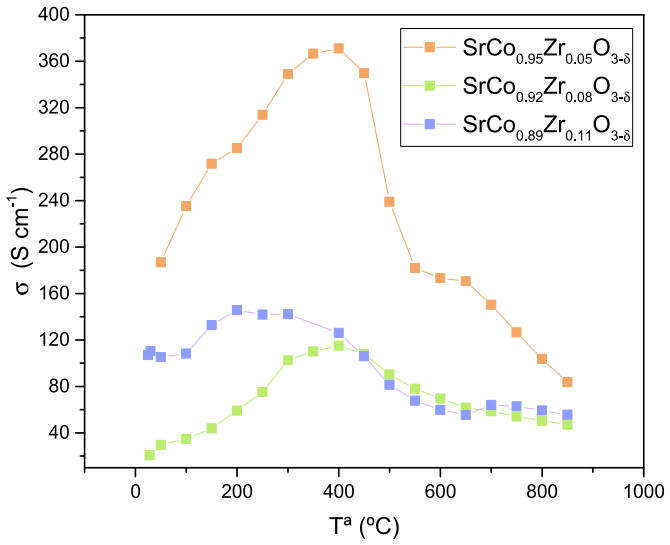

Fig. 6. DC-conductivity as a function of temperature for $SrCo_{1-x}Zr_xO_{3-\delta}$ (x = 0.05, 0.08 and 0.11).

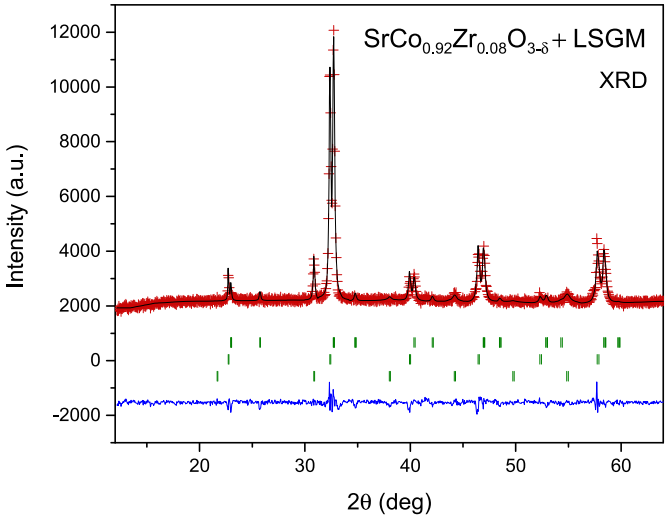

Fig. 7. Rietveld-refined XRD profile of a mixture of LSGM and $SrCo_{0.92}Zr_{0.08}O_{3-\delta}$ after a thermal treatment at 900 °C in air for 12 h, showing no reaction products between both phases other than the initial products. The first and second series of Bragg positions (green lines) correspond to $SrCo_{0.92}Zr_{0.08}O_{3-\delta}$ and LSGM, respectively while the third series (green lines) corresponds to the impurity of $SrZrO_3$. (For interpretation of the references to colour in this figure legend, the reader is referred to the Web version of this article.)

$Sr(NO_3)_2$ (99%; Sigma-Aldrich), $Co(NO_3)_2.6H_2O$ (98%; Alfa Aesar) and $ZrO(NO_3)_2 \cdot 6H_2O$ (99,9%; Sigma-Aldrich), were mixed and dissolved in an aqueous solution containing 10% citric acid. The solution was evaporated at a temperature of 300 °C, leading to the formation of a gel-like substance. This gel was subjected to decomposition for 12 h at temperatures reaching up to 600 °C. Subsequently, two additional heating steps were carried out; firstly at 1000 °C for 24 h, and after grinding the powders, they were heated during 12 h at 1100 °C.

The identification and assessment of phase purity of the reaction products were conducted using XRD. XRD patterns were collected using a Bruker D8 Advance diffractometer (40 kV, 30 mA) operating under DIFFRACT^{PLUS} software, employing Bragg−Brentano reflection geometry. CuK_α radiation ($\lambda = 1.540$ Å) and a position-sensitive detector (PSD) were utilized, with a nickel filter employed to eliminate CuK_β radiation. The XRD patterns were acquired in the 2θ range of 12–64° for phase

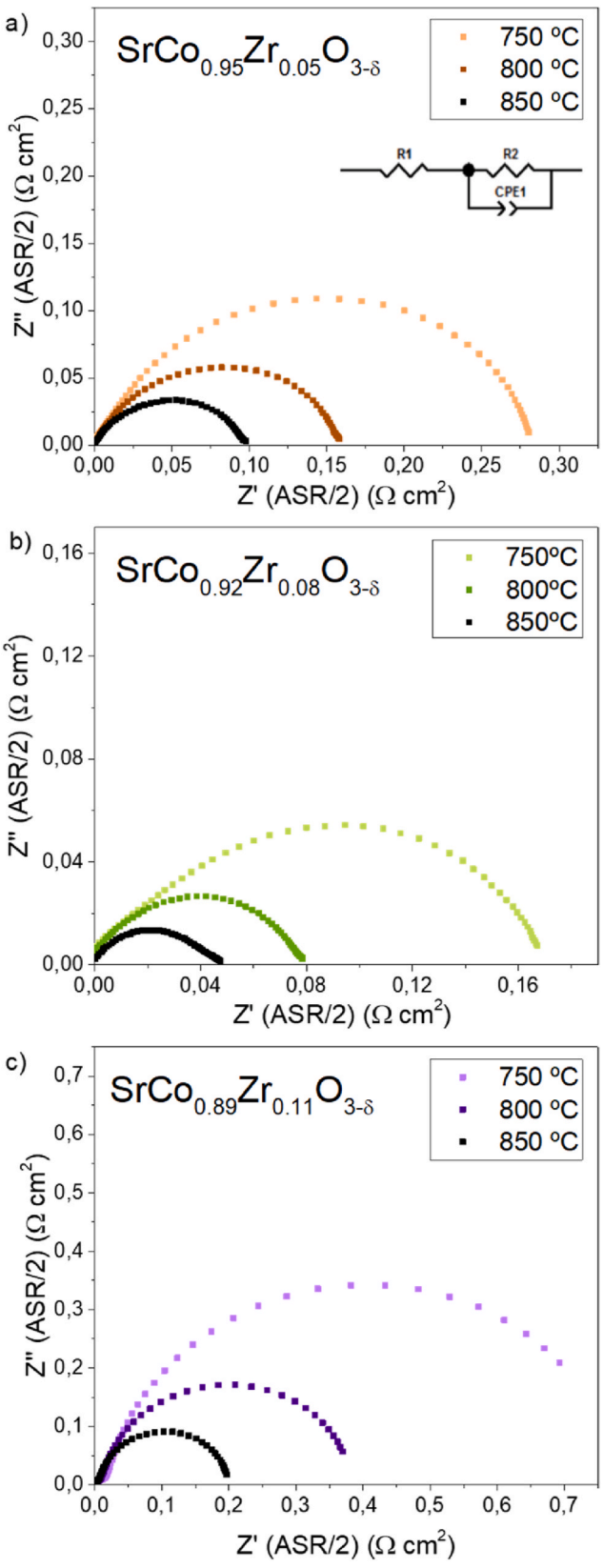

Fig. 8. Electrochemical impedance spectra obtained at 750, 800 and 850 °C in a symmetrical cell supported on LSGM electrolyte for a) $SrCo_{0.95}Zr_{0.05}O_{3-\delta}$, b) $SrCo_{0.92}Zr_{0.08}O_{3-\delta}$ and c) $SrCo_{0.89}Zr_{0.11}O_{3-\delta}$. The inset in a) shows the equivalent circuit employed for fitting the experimental data.

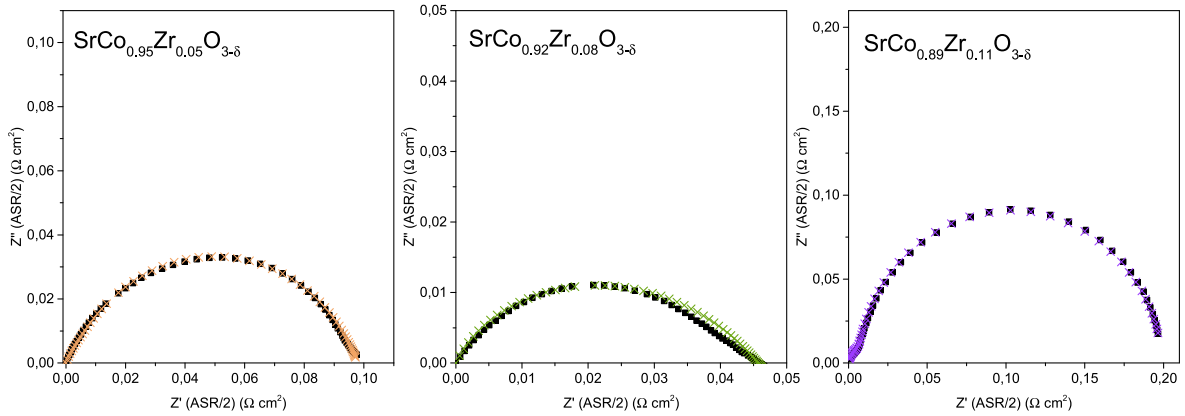

Fig. 9. Fitting of the electrochemical impedance curves obtained at 850 °C in a symmetrical cell supported on LSGM electrolyte for $SrCo_{0.95}Zr_{0.05}O_{3-\delta}$, $SrCo_{0.92}Zr_{0.08}O_{3-\delta}$ and $SrCo_{0.89}Zr_{0.11}O_{3-\delta}$. Fitted lines for each curve are depicted in distinct colours: orange, green, or purple. (For interpretation of the references to colour in this figure legend, the reader is referred to the Web version of this article.)

identification and purity evaluation. Furthermore, this XRD methodology was employed to investigate the compatibility of the reaction products with the LSGM electrolyte.

A NPD study carried out at 25 °C at the Laue Langevin Institute (ILL) in Grenoble, France, was also essential for a comprehensive characterization of the crystal structure, particularly regarding oxygen vacancy content and distribution. The Two-Axis High-Resolution Diffractometer (D2B) was employed for this measurement; the coherent neutron scattering factors (fm) for the sample elements are as follows: Sr (7.02), Co (2.49), Zr (7.16), and O (5.803) [24]. Neutron diffraction measurements were conducted using a wavelength (λ) of 1.594 Å, covering an angular range from 0 to 160°. One gram of the synthesized polycrystalline material was placed on a vanadium sample holder. The obtained pattern was analysed using the Rietveld method [25], with FULLPROF [26] refinement software. A pseudo-Voigt function was selected to generate the line profile of the diffraction peaks. In the final analysis, various parameters were refined, including the scale factor, background points, zero shift, half-width, pseudo-Voigt parameters adjusted for asymmetry, unit-cell parameters, positional coordinates, isotropic displacement factors for Sr, Co, Zr and O1 atoms, and anisotropic factors for O2 and O3 oxygen atoms.

For the thermogravimetric analysis (TGA) of $SrCo_{1-x}Zr_xO_{3-\delta}$ (x = 0.05, 0.08 and 0.11), about 50 mg of the sample underwent heating up to 900 °C. The analysis was conducted under an oxygen atmosphere using a Thermal Analysis SDT Q-600 instrument. For determining the thermal expansion coefficient (TEC), a dilatometric analysis was performed on cylindrical pellets with 5 mm diameter and 2 mm thickness, using approximately 0.25 g of the samples. These pellets were subjected to thermal treatment at 1100 °C for 12 h. Measurements were carried out using a LINSEIS L75/H dilatometer in an air environment, spanning from 25 to 900 °C.

Electrical conductivity measurements were performed using the four-point probe method on rectangular pellets (10x3x3mm). These pellets, weighing approximately 0.3 g each, were sintered at 1100 °C for 12 h. Following that, four platinum wires were attached to them, securing them with drops of platinum ink. To cure it, the pellets were placed in a furnace at 850 °C for 1 h. Subsequently, the pellets were positioned in an alumina holder within the ProboStat for the measurement of their electrical conductivity. The measurements were conducted using an AUTOLAB PGSTAT 302, ECHO CHEMIE system, spanning a temperature range from 25 to 850 °C.

A chemical compatibility study between the $SrCo_{1-x}Zr_xO_{3-\delta}$ (x = 0.05, 0.08 and 0.11) samples and the electrolyte $La_{0.80}Sr_{0.20}Ga_{0.83}Mg_{0.17}O_{3-\delta}$ (LSGM) was carried out. Stoichiometric amounts of both materials were mixed and heated at 900 °C for 12 h in air, and then identified using XRD with a Bruker D8 Advance diffractometer.

For AC impedance measurements, an 11 mm diameter and 2 mm thick LSGM pellet was used. This pellet was then heated to 1450 °C for 20 h after it was pressed. With the use of ink made from a cathode solution combined with terpineol, the cathode was applied to both sides of the electrolyte pellet. The cathode and electrolyte were calcined at 1000 °C for 4 h to guarantee adherence. Then, platinum ink was applied to both surfaces, followed by a similar calcination procedure that lasted for 2 h at 900 °C. These tests were performed using an AUTOLAB system that is computer controlled and has a PSTAT30 potentiostat and a FRA2 frequency analyzer from Eco Chemie B.V. The measurements were performed within a temperature range of 750–850 °C in an air atmosphere, using a vertical tubular furnace.

Single cell tests were carried out assembling a real fuel cell consisting of the $SrCo_{1-x}Zr_xO_{3-\delta}$ (x = 0.05, 0.08 and 0.11) cathodes, LSGM electrolyte, and the anode $SrMo_{0.8}Fe_{0.2}O_{3-\delta}$ [27]. To assess the performance of the manufactured cathodic samples, the cell was supported on the electrolyte (in this case, 300 μm thick LSGM). The SMART CUT LP was used to polish the sintered LSGM pellets (16.5 x 2 mm). In order to stop ionic interdiffusion between the electrolyte and the anode, a buffer-layer ink of composition $La_{0.4}Ce_{0.6}O_{2-\delta}$ ("lanthanum-doped ceria" LDC) was then applied as a layer (0.5 cm x 0.5 cm) on one side. It was subsequently heated to 1300 °C for an hour in a furnace. An anode ink layer with the same dimensions was applied on top of the buffer layer, and it was heated to 1100 °C for an hour. Subsequently, the cathode ink was applied to the other side of the electrolyte pellet. The cathode-electrolyte adhesion was achieved by calcining them for 1 h at 1100 °C. To prepare each ink, a Retsch PM 100 planetary mill was used to grind the respective compound powders (cathodes, anodes, or buffer-layer) for 1 h at 450 rpm and a few drops of terpineol were then added. A platinum mesh with a crossed thread of the same element was placed over the anode and cathode as current collectors. The mesh was fixed with platinum ink at 850 °C for 1 h. The single cell electrodes had a working surface of 0.25 cm^2 (0.5 cm x 0.5 cm). The pellet was then heated to the operating temperature of 800 and 850 °C and placed in an alumina tube to function as a fuel cell in a vertical tubular furnace. As the temperature increases, a 5% H_2 stream was directed through the anode to convert the oxide to its active perovskite phase. Specifically, within the temperature range of 800–850 °C, pure H_2 was employed. The instrument utilized for acquiring current-voltage curves was the AUTOLAB 302 N Potentiostat-Galvanostat. To evaluate the performance of the single cell, current-voltage curves were generated, and the corresponding power density was calculated by multiplying voltage and current density.

Scanning electron microscopy (SEM) images were collected with a table-top Hitachi TM-1000 microscope.

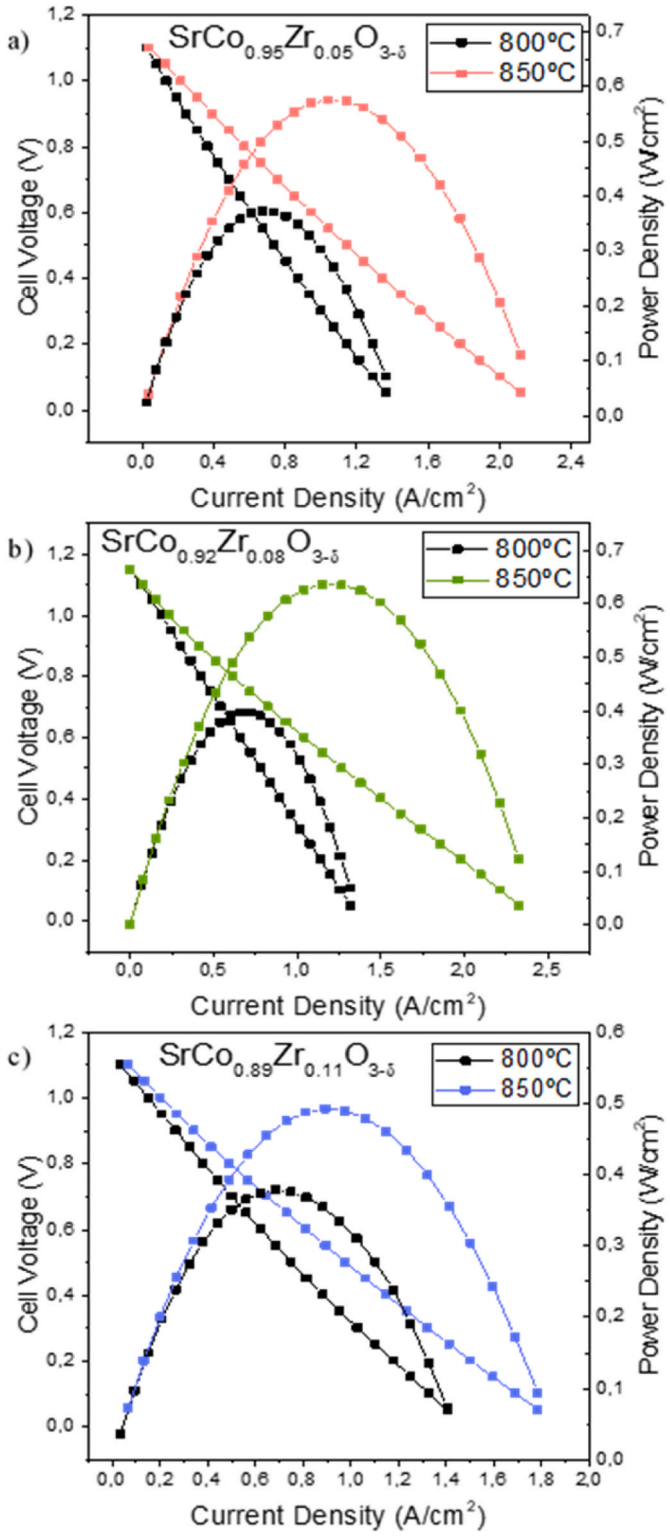

Fig. 10. Cell voltage (left axis) and power density (right axis) as a function of current density for the test cell with the configuration $SrCo_{1-x}Zr_xO_{3-\delta}$/LSGM/LDC/SMFO in pure H_2 measured at 850 and 800 °C being a) $SrCo_{0.95}Zr_{0.05}O_{3-\delta}$ b) $SrCo_{0.92}Zr_{0.08}O_{3-\delta}$ and c) $SrCo_{0.89}Zr_{0.11}O_{3-\delta}$.

3. Result and discussion

3.1. Crystallographic characterization

Fig. 1 shows the XRD patterns at room temperature for $SrCo_{1-x}Zr_xO_{3-\delta}$ (x = 0.05, 0.08 and 0.11), alongside the undoped $SrCoO_{3-\delta}$. The zirconium-doped samples exhibit a predominant tetragonal perovskite phase with excellent crystallinity. A secondary phase ($Sr_2Co_2O_5$) with a brownmillerite structure defined in the *Imma* space group was found in the cathodes of smaller zirconium content. However, as the doping increased, this secondary phase disappeared, and it is not visible in $SrCo_{0.89}Zr_{0.11}O_{3-\delta}$. Additionally, a minor impurity of $SrZrO_3$, indicated by # in Fig. 1, was found in the three samples. In contrast, the undoped cathode of $SrCoO_{3-\delta}$ shows an undesired 2H hexagonal phase. These results highlight that even a modest 5% Zr content completely prevents the formation of the unwanted hexagonal phase. Moreover, the tetragonal perovskite phase persists as the Zr content increases up to 11%.

Table 2
Comparison of the power-density values of single fuel cells for other systems belonging to the $SrCo_{1-x}M_xO_{3-\delta}$ family (M = Nb, Ti, Ru, V, Ir), at 850 °C.

Cathodes reported in bibliography	Power Density at 850 °C (mW/cm²)
[33]$SrCo_{0.85}Nb_{0.15}O_{3-\delta}$	550
[18]$SrCo_{0.85}Ti_{0.15}O_{3-\delta}$	614
[19]$SrCo_{0.9}Ru_{0.1}O_{3-\delta}$	652
[32]$SrCo_{0.97}V_{0.03}O_{3-\delta}$	550
[17]$SrCo_{0.95}Nb_{0.05}O_{3-\delta}$	600
$SrCo_{0.95}Zr_{0.05}O_{3-\delta}$	575 (This work)
$SrCo_{0.92}Zr_{0.08}O_{3-\delta}$	636 (This work)
$SrCo_{0.89}Zr_{0.11}O_{3-\delta}$	492 (This work)

A NPD study at Room Temperature (RT) played a crucial role in elucidating structural features of the synthesized $SrCo_{0.89}Zr_{0.11}O_{3-\delta}$ perovskite (Fig. 2). The collected NPD diagram revealed a superstructure with doubled *c* axis, as $a = b \approx a_0$, $c \approx 2a_0$. The crystal structure model was defined in the tetragonal *P4/mmm* (No. 123) space group. Sr atoms occupy the 2*h* sites (1/2,1/2, z); Co is distributed in the 1*a* (0,0,0) and 1*b* (0,0,1/2) positions, with the latter (1*b*) also hosting Zr atoms ((Co,Zr)2), and three types of oxygen atoms, O1 at 2*f* (1/2,0,0), O2 at 2*g* (0,0,z), and O3 at 2*e* (1/2,0,1/2). The occupancy factors for the three types of oxygen were also refined, revealing a concentration of vacancies primarily at the O3 position (f_{occ} O3 = 0.782). After the full refinement, a crystallographic formula of $SrCo_{0.89}Zr_{0.11}O_{2.772(1)}$ was derived from the NPD data. Fig. 2 illustrates the goodness of the fit for the NPD pattern. Notably, the room temperature NPD pattern displays a systematic splitting of the diffraction peaks, more noticeable at high scattering angles. While not evident in laboratory XRD patterns, this splitting is discernible in the NPD diagram due to its exceptionally high angular resolution. This splitting is attributed to the presence of two distinct perovskite phases, with notable differences in unit-cell parameters and Zr distribution. An initial analysis already shows that the first phase (with higher *a* and *c* unit-cell parameters, as well as superior Zr content at the (Co,Zr)2 site) gives rise to broader reflections, whereas the second phase (with smaller *a* and *c* value) exhibits narrower peaks, corresponding to larger scattering domains. The disorder introduced by this phase segregation may be beneficial for its performance as cathode. Several studies on high-entropy cathodes, where several metal species are introduced in perovskite or double perovskite structures experimentally show that these materials exhibited lower TEC, suppressed strontium surface segregation [28] as well as more stable polarisation resistance, showing outstanding output performances [29].

Table 1 lists the main refined parameters, including occupation factors of the doping Zr atoms, independently refined for each phase, unit-cell parameters, atomic positions, reliability factors as well as the bond distances of $SrCo_{0.92}Zr_{0.08}O_{2.76}$ and $SrCo_{0.97}Zr_{0.03}O_{2.76}$.

Fig. 3 displays a schematic view of the tetragonal crystal structure obtained for $SrCo_{0.89}Zr_{0.11}O_{3-\delta}$ perovskite. In this tetragonal superstructure, elongated Co2 octahedra can be seen exhibiting significant axial distortion with four shorter Co2–O3 equatorial distances and two longer axial distances Co2–O2. In contrast, flattened Co1 octahedra was found possessing extremely short Co1–O2 distances. This

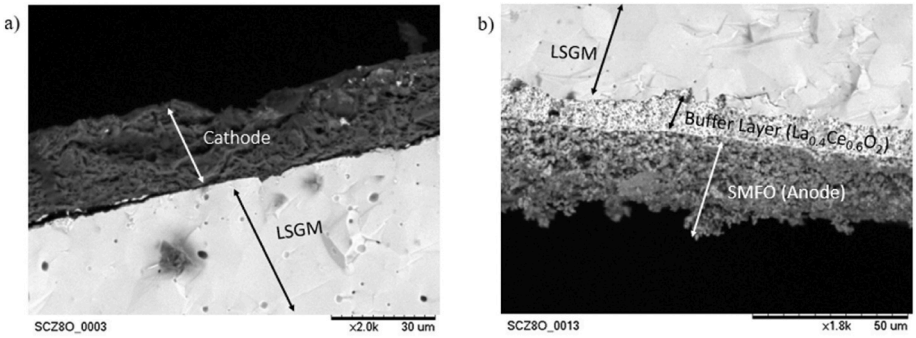

Fig. 11. SEM micrograph showing a) the porous cathode layer of $SrCo_{0.92}Zr_{0.08}O_{3-\delta}$ fully adhered to the dense LSGM electrolyte, and b) the SMFO anode layer and buffer layer adhered to the LSGM electrolyte.

phenomenology might suggest that Co1 cations could present a higher oxidation state than Co2. This hypothesis implies a mixed oxidation state of $Co^{3+}/^{4+}$ at Co1 positions and Co^{3+} at Co2 positions, assuming a completely disproportionate charge. Additionally, to characterize the thermal displacements of oxygen atoms, anisotropic thermal vibrations of O2 and O3 were incorporated. The equatorial O3 atoms display thermal displacements in the form of elongated, cigar-shaped ellipsoids, with long axis perpendicular to the Co–O–Co direction (Fig. 3). This observation may indicate a dynamic tilting of the $Co2O_6$ octahedra, potentially hinting at the migration of oxygen vacancies along the c axis, leading to alterations in the O–O distances along this direction. In contrast, axial O2 oxygen atoms exhibit flat ellipsoids with significantly less anisotropy, with the short axes of the ellipsoids oriented along the bonding direction.

Two magnetic peaks were observed at room temperature in the NPD pattern (Fig. 2). These peaks suggest that the sample is magnetically ordered above room temperature. The magnetic structure was fully developed at this temperature. A propagation vector $k = (1/2,1/2,0)$ was identified. A G-type magnetic structure perfectly fits the magnetic intensities. In this spin arrangement (inset of Fig. 2) each Co magnetic moment is antiferromagnetically coupled to 6 Co neighbors. The values of the refined magnetic moments are included in Table 1.

3.2. Thermogravimetric analysis (TGA)

A study of the weight evolution of $SrCo_{1-x}Zr_xO_{3-\delta}$ (x = 0.05, 0.08 and 0.11) phases has been carried out at different temperatures under an oxygen atmosphere. In Fig. 4, the thermogravimetric curves of the synthesized compounds are presented. Notably, around 400 °C, a change in slope is observed, likely indicative of a phase transition from tetragonal to cubic, a phenomenon observed in other cobalt-doped compounds reported in the literature [18,21]. For $SrCo_{0.95}Zr_{0.05}O_{3-\delta}$, a total weight loss of 0.83% is observed, corresponding to the loss of 0.10 oxygen atoms per formula. In the case of $SrCo_{0.92}Zr_{0.08}O_{3-\delta}$ and $SrCo_{0.89}Zr_{0.11}O_{3-\delta}$, total losses of 1.21% and 1.10%, respectively, are noted, corresponding to 0.15 and 0.13 oxygen atoms per formula.

In fact, the global observed weight loss in the TG curves is the result of a compromise between two effects. On one hand, for intermediate x = 0.08 Zr doping, the introduction of Zr^{4+} ions into the crystal structure of the perovskite oxide, involves an increment in the oxygen content in the stating perovskite (at RT). This increment, upon heating, is able to deliver a superior amount of lattice oxygen at higher temperatures (up to 900 °C); on the other hand, this effect is partially masked for x = 0.11 by the presence of substantial amounts of $SrZrO_3$ impurity, which is thermally stable and does not contribute to the observed weight loss. In any case, based on previous studies [18], the observed weight losses suggest that at the operating temperatures of solid oxide fuel cells, $SrCo_{1-x}Zr_xO_{3-\delta}$ (x = 0.05, 0.08 and 0.11) cathode materials exhibit an increased oxygen deficiency, thereby enhancing the movement of O^{2-} ions through the structure via a vacancy mechanism.

3.3. Thermal expansion measurements

A dilatometric study has been conducted to assess the mechanical compatibility of $SrCo_{1-x}Zr_xO_{3-\delta}$ (x = 0.05, 0.08 and 0.11) cathode materials with respect to the other components of the cell. Thermal expansion measurements were performed on the sintered pellets in an air atmosphere from 200 to 900 °C.

The thermal expansion measurements of $SrCo_{1-x}Zr_xO_{3-\delta}$ (x = 0.05, 0.08, and 0.11) are presented in Fig. 5. The resulting thermal expansion coefficients (TECs), measured between 400 and 850 °C, were found to be $14.27{\cdot}10^{-6}$, $18.24{\cdot}10^{-6}$ and $19.46{\cdot}10^{-6}$ K^{-1} for x values of 0.05, 0.08 and 0.11, respectively. The slight variation in the slope registered around 400 °C, could be related to the tetragonal-to-cubic phase transition as seen in Refs. [18,21]. This change in slope aligns with the same observation in the thermogravimetric analysis at the same temperature.

The TEC for $SrCo_{0.95}Zr_{0.05}O_{3-\delta}$ is highly favourable, especially when considering the value of the electrolyte employed ($TEC_{LSGM} = 12.5{\cdot}10^{-6}$ K^{-1}) [30]. It is observed that an increase in the Zr content leads to a rise in the TEC value. Although the thermal expansion coefficients of the compounds are slightly higher than that of the electrolyte, they remain lower than the typical values found in many cobalt perovskites, which often exceed $20{\cdot}10^{-6}$ K^{-1} as it is reported for iridium-doped cathodes ($SrCo_{0.90}Ir_{0.10}O_{3-\delta}$ (TEC = $24.35{\cdot}10^{-6}$ K^{-1}) and $SrCo_{0.85}Ir_{0.15}O_{3-\delta}$ (TEC = $24.33{\cdot}10^{-6}$ K^{-1})) or in the case of $SrCo_{0.50}Fe_{0.45}Ti_{0.05}O_{3-\delta}$ (TEC = $23.49{\cdot}10^{-6}$ K^{-1}) [21,31].

3.4. Electrical conductivity measurements and chemical compatibility

The electrical conductivity of $SrCo_{1-x}Zr_xO_{3-\delta}$ (x = 0.05, 0.08 and 0.11) has been determined using the four-probe method in air, within a temperature range from 25 to 850 °C under direct current. Fig. 6 illustrates a semiconductor behavior in the temperature range of 25–400 °C for 5 %, 8% and 11% Zirconium-doped samples. Above 400 °C, a metal-insulator transition occurs, with a maximum conductivity of 84 S cm^{-1} at 850 °C for $SrCo_{0.95}Zr_{0.05}O_{3-\delta}$, 59 S cm^{-1} for $SrCo_{0.92}Zr_{0.08}O_{3-\delta}$ and 56 S cm^{-1} for $SrCo_{0.89}Zr_{0.11}O_{3-\delta}$ at 850 °C (the working temperature of a SOFC). This change in conductivity behavior coincides with the observed change in slope in both thermogravimetric and dilatometric analysis at the same temperature, providing additional support for structural transition from tetragonal to cubic occurring around that temperature.

A detailed neutron diffraction study across the whole temperature range below 900 °C would be required to unveil the correlation between the conductivity evolution and subtle structural changes, which is currently lacking. However, by comparison with similar systems with $SrCo_{1-x}Ir_xO_{3-\delta}$ compositions [20,21], it can be inferred that i) at about 400 °C a phase transition from tetragonal for cubic is observed, clearly correlated to the change of conduction regime (with a maximum in conductivity at 400 °C). This transition involves the disordering of oxygen vacancies in a cubic perovskite structure and ii) in the 500–700 °C

temperature range, the rate of oxygen loss of the materials abruptly increases, yielding very defective perovskite structures where oxygen diffusion is enhanced. This increment of the oxygen non-stoichiometry may affect the electronic conductivity in the same temperature range, accounting for the observed anomalies shown in Fig. 5.

A decrease in the electrical conductivity is observed with an increase in Zr-content, likely attributed to the presence of Zr^{4+} ions that perturbs the path for electronic conduction through Co–O–Co bonds. Moreover, it cannot be discarded that the presence of increasing amounts of $SrZrO_3$ impurity, which is an insulator, for x = 0.08, 0.11, probably contribute to the overall decrease in conductivity observed in Fig. 6. Nevertheless, the obtained electrical conductivities for the compounds are sufficient for successful use of these materials as cathodes in a SOFC [32].

Fig. 7 displays the structural Rietveld refinement of the X-ray diffraction pattern of $SrCo_{0.92}Zr_{0.08}O_{3-\delta}$ mixed with LSGM after treatment at 900 °C for 12 h. No evidence of a possible chemical reaction between these compounds was observed. The diffraction reflections correspond to three crystallographic phases: the pristine $SrCo_{0.92}Zr_{0.08}O_{3-\delta}$ material, together with the $SrZrO_3$ impurity and those of the LSGM, demonstrating their chemical compatibility at the operating temperatures of a SOFC. Similar chemical compatibility results were obtained for $SrCo_{0.95}Zr_{0.05}O_{3-\delta}$ and $SrCo_{0.89}Zr_{0.11}O_{3-\delta}$ with the electrolyte.

3.5. Electrochemical impedance spectroscopy (EIS) results

The polarisation resistance of $SrCo_{1-x}Zr_xO_{3-\delta}$ (x = 0.05, 0.08 and 0.11) samples was analysed by AC complex impedance spectroscopy measurements in symmetrical cells with LSGM as electrolyte (Fig. 8).

As expected, the resistance decreases as the temperature increases. All impedance diagrams were normalized by the superficial area, and the R parameters obtained in the fitting for each process were divided by two to account for the contribution of both electrodes. The contribution of the electrolyte is taken into account by the introduction of a series resistor (R1) in the equivalent circuit used to fit the experimental data, while the polarisation process is simulated by a series of RP-CPE elements (R2, CPE1) (inset in Fig. 8a). This fitting is shown in Fig. 9 for $SrCo_{1-x}Zr_xO_{3-\delta}$ (x = 0.05, 0.08 and 0.11) at 850 °C. The same procedure was used for 800 and 750 °C. The represented spectra have been shifted from the origin of the Z-axis after subtracting the ohmic resistance of the electrolyte in order to make a simpler comparison of the polarisation processes of samples at the different temperatures.

For the $SrCo_{0.95}Zr_{0.05}O_{3-\delta}$ cathode (Fig. 8a), polarisation resistances of 0.281, 0.158 and 0.097 Ω cm^2 at 750, 800 and 850 °C, respectively, are observed; while for $SrCo_{0.92}Zr_{0.08}O_{3-\delta}$ (Fig. 8b), polarisation resistances of 0.167, 0.078 and 0.047 Ω cm^2 at 750, 800 and 850 °C, respectively, have been obtained. These values are significantly better than those described in previous works for cathode materials with $SrCoO_{3-\delta}$ derived compositions (for instance, for $SrCo_{0.90}Ru_{0.10}O_{3-\delta}$: 0.11 Ω cm^2 at 850 °C or for $SrCo_{0.90}Ir_{0.10}O_{3-\delta}$: 0.07 Ω cm^2 at 850 °C) [19,21], contributing to the adequate performance of these compounds as cathodes in IT-SOFCs. For the $SrCo_{0.89}Zr_{0.11}O_{3-\delta}$ cathode (Fig. 8c) slightly higher values were obtained, with polarisation resistances of 0.69, 0.369 and 0.1965 Ω cm^2 at 750, 800 and 850 °C, respectively. It seems that the excessive Zr doping reduced the electrochemical performance; although the presence of Zr cations is necessary to stabilize the desired tetragonal or cubic phases, an excessive Zr doping correspondingly decreases the amount of Co, which is the active element with excellent catalytic characteristics and, then, $SrCo_{0.92}Zr_{0.08}O_{3-\delta}$ shows optimum properties. Nevertheless, these higher values are still comparable with others obtained in similar materials that successfully performed as good cathodes in SOFC [15].

3.6. Fuel-cell evaluation

To assess the efficiency of the $SrCo_{1-x}Zr_xO_{3-\delta}$ (x = 0.05, 0.08 and 0.11) cathodes in testing SOFCs, tests were conducted using a single cell that was supported by a 300-micron-thick LSGM electrolyte, with $SrMo_{0.8}Fe_{0.2}O_{3-\delta}$ (SMFO) serving as the anode.

In Fig. 10.a, the corresponding performance for the $SrCo_{0.95}Zr_{0.05}O_{3-\delta}$ cathode at 800 and 850 °C is depicted, with maximum power densities of 372 and 575 mW cm^{-2}, respectively. Fig. 10.b illustrates the power curve of the $SrCo_{0.92}Zr_{0.08}O_{3-\delta}$ single cell at 800 and 850 °C, achieving a maximum power density of 397 and 636 mW cm^{-2}. This increase is expected based on the results of complex impedance measurements compared to the $SrCo_{0.95}Zr_{0.05}O_{3-\delta}$ single cell. Finally, in Fig. 10.c, the cell voltage and power density are presented as a function of current density at 800 and 850 °C for the latter $SrCo_{0.89}Zr_{0.11}O_{3-\delta}$ zirconium cathode, operated with pure H_2. The maximum power densities obtained are 378 and 492 mW cm^{-2}, respectively.

Table 2 includes the power densities obtained at 850 °C for cathodes reported in the literature under the same conditions, using the same anode (SMFO) and electrolyte (LSGM) with the same thickness. When comparing the cathodes synthesized in this work with those reported in the bibliography, it is observed that $SrCo_{0.92}Zr_{0.08}O_{3-\delta}$ (636 mW/cm^2) is similar in performance to the best cathode material, $SrCo_{0.9}Ru_{0.1}O_{3-\delta}$.

3.7. Post-mortem SEM study

Fig. 11.a illustrates the micrograph of the cross-section view of the $SrCo_{0.92}Zr_{0.08}O_{3-\delta}$ cathode-electrolyte interface after the single-cell test, analysed by scanning electron microscopy (SEM). $SrCo_{0.92}Zr_{0.08}O_{3-\delta}$ layer has a thickness of about 20–25 μm, exhibits good porosity, an essential requirement for optimal cathodic materials, as it promotes the diffusion and reduction process of air throughout the cathode layer. Additionally, Fig. 11.a shows a uniform and dense electrolyte layer, without cracks or fractures. No formation of fractures or delamination between the electrode and the electrolyte were observed after the single-cell test. In Fig. 11.b, the opposite side of the cell can be observed, showing the anode and the intermediate buffer-layer adhered to the electrolyte, with an estimated thickness of about 10–15 μm. Similar characteristics are observed regarding porosity, uniformity, and degree of adhesion.

These conditions required for its performance as cathodic materials do not appear to degrade after operating at 850 °C during the single-cell tests.

4. Conclusion

In this work, $SrCo_{1-x}Zr_xO_{3-\delta}$ (x = 0.05, 0.08 and 0.11) perovskites have been successfully synthesized and implemented as cathode material in solid oxide fuel cells. The exceptional performance is proven by maximum power densities of 636 mW/cm^2 at 850 °C with pure H_2 as fuel, in $SrCo_{0.92}Zr_{0.08}O_{3-\delta}$. The positive outcomes observed in single-cell tests are attributed to the structural features, analysed from room temperature X-ray diffraction and neutron powder diffraction at RT. The crystal structure has been refined at RT in the *P4/mmm* space group. It corresponds to a perovskite superstructure with a doubled *c* axis, due to the long-range ordering of layers of significantly deficient O3 oxygen sites. It also displays a systematic splitting of diffraction peaks. The disorder introduced by the observed phase segregation is beneficial for reducing the polarisation resistance and boosting the power output, similar to what is described for high-entropy cathode materials.

The thermal expansion coefficients (TEC) for these perovskites are well-matched with the commonly used electrolyte (LSGM). Despite a slightly higher thermal expansion coefficient for $SrCo_{0.92}Zr_{0.08}O_{3-\delta}$, the transport properties make it a promising alternative as a cathode in intermediate temperature solid oxide fuel cells. The studied perovskites show a semiconducting behavior with a subsequent metal-insulator transition with conductivity values between 56 and 84 S cm^{-1} at the operating temperatures. Notably, polarisation resistances for symmetrical cells show low ASR values, reaching 0.047 and 0.078 Ω cm^2 at 800

and 850 °C for the $SrCo_{0.92}Zr_{0.08}O_{3-\delta}$ cathode, respectively. Finally, a post-mortem SEM study confirmed that the cathodic materials exhibited no degradation after operating at 850 °C during single-cell tests.

CRediT authorship contribution statement

Mónica Chivite-Lacaba: Investigation, Writing – original draft, Formal analysis. **Jesús Prado-Gonjal:** Formal analysis, Investigation, Supervision, Writing – review & editing. **José Antonio Alonso:** Formal analysis, Funding acquisition, Investigation, Supervision, Writing – review & editing, Conceptualization, Resources. **María Teresa Fernández-Díaz:** Investigation, Writing – review & editing. **Vanessa Cascos:** Conceptualization, Formal analysis, Funding acquisition, Investigation, Resources, Supervision, Writing – review & editing.

Declaration of competing interest

The authors declare that they have no known competing financial interests or personal relationships that could have appeared to influence the work reported in this paper.

Acknowledgments

JAA thanks the financial support of the MCIN for funding the project number: PID2021-122477OB-I00 and TED2021-129254B–C22. We acknowledge the Institut Laue-Langevin (ILL) for making all facilities available. VC and JPG thank to the MCIN (MCIN/AEI/10.13039/501100011033) for granting the project PID2020-112848RB-C21. VC appreciates the support of Community of Madrid - Universidad Complutense de Madrid for the concession of the project PR27/21-002 and for granting the "Atracción de Talento program" fellowship, 2019- T2/IND-13483.

References

[1] Z. Zakaria, S.H. Abu Hassan, N. Shaari, A.Z. Yahaya, Y. Boon Kar, A review on recent status and challenges of yttria stabilized zirconia modification to lowering the temperature of solid oxide fuel cells operation, Int. J. Energy Res. 44 (2020) 631–650, https://doi.org/10.1002/er.4944.

[2] M.S. Arshad, R. Raza, M.A. Ahmad, G. Abbas, A. Ali, A. Rafique, M.K. Ullah, S. Rauf, M.I. Asghar, N. Mushtaq, S. Atiq, S. Naseem, An efficient Sm and Ge co-doped ceria nanocomposite electrolyte for low temperature solid oxide fuel cells, Ceram. Int. 44 (2018) 170–174, https://doi.org/10.1016/j.ceramint.2017.09.155.

[3] L. Fan, B. Zhu, P.-C. Su, C. He, Nanomaterials and technologies for low temperature solid oxide fuel cells: recent advances, challenges and opportunities, Nano Energy 45 (2018) 148–176, https://doi.org/10.1016/j.nanoen.2017.12.044.

[4] Y. Song, Y. Chen, W. Wang, C. Zhou, Y. Zhong, G. Yang, W. Zhou, M. Liu, Z. Shao, Self-assembled triple-conducting nanocomposite as a superior Protonic ceramic fuel cell cathode, Joule 3 (2019) 2842–2853, https://doi.org/10.1016/j.joule.2019.07.004.

[5] M.K. Singla, P. Nijhawan, A.S. Oberoi, Hydrogen fuel and fuel cell technology for cleaner future: a review, Environ. Sci. Pollut. Control Ser. 28 (2021) 15607–15626, https://doi.org/10.1007/s11356-020-12231-8.

[6] N. Laosiripojana, W. Wiyaratn, W. Kiatkittipong, A. Arpornwichanop, A. Soottitantawat, S. Assabumrungrat, Reviews on solid oxide fuel cell technology, Eng. J. 13 (2009) 65–84, https://doi.org/10.4186/ej.2009.13.1.65.

[7] D.J.L. Brett, A. Atkinson, N.P. Brandon, S.J. Skinner, Intermediate temperature solid oxide fuel cells, Chem. Soc. Rev. 37 (2008) 1568, https://doi.org/10.1039/b612060c.

[8] E.D. Wachsman, K.T. Lee, Lowering the temperature of solid oxide fuel cells, Science (1979) 334 (2011) 935–939, https://doi.org/10.1126/science.1204090.

[9] G. Yang, C. Su, H. Shi, Y. Zhu, Y. Song, W. Zhou, Z. Shao, Toward reducing the operation temperature of solid oxide fuel cells: Our Past 15 Years of efforts in cathode development, Energy Fuel. 34 (2020) 15169–15194, https://doi.org/10.1021/acs.energyfuels.0c01887.

[10] W. Yang, T. Hong, S. Li, Z. Ma, C. Sun, C. Xia, L. Chen, Perovskite $Sr_{1-x}Ce_xCoO_{3-\delta}$ ($0.05 \leq x \leq 0.15$) as superior cathodes for intermediate temperature solid oxide fuel cells, ACS Appl. Mater. Interfaces 5 (2013) 1143–1148, https://doi.org/10.1021/am3029238.

[11] W. Yang, H. Zhang, C. Sun, L. Liu, J.A. Alonso, M.T. Fernández-Díaz, L. Chen, Insight into the structure and functional application of the $Sr_{0.95}Ce_{0.05}CoO_{3-\delta}$ cathode for solid oxide fuel cells, Inorg. Chem. 54 (2015) 3477–3484, https://doi.org/10.1021/acs.inorgchem.5b00051.

[12] A. Esquirol, N.P. Brandon, J.A. Kilner, M. Mogensen, Electrochemical characterization of $La_{0.6}Sr_{0.4}Co_{0.2}Fe_{0.8}O_3$ cathodes for intermediate-temperature SOFCs, J. Electrochem. Soc. 151 (2004) A1847, https://doi.org/10.1149/1.1799391.

[13] S. Wang, Performance of a $La_{0.6}Sr_{0.4}Co_{0.8}Fe_{0.2}O_3$-$Ce_{0.8}Gd_{0.2}O_{1.9}$–Ag cathode for ceria electrolyte SOFCs, Solid State Ionics 146 (2002) 203–210, https://doi.org/10.1016/S0167-2738(01)01015-3.

[14] S. Wang, M. Katsuki, M. Dokiya, T. Hashimoto, High temperature properties of $La_{0.6}Sr_{0.4}Co_{0.8}Fe_{0.2}O_{3-\delta}$ phase structure and electrical conductivity, Solid State Ionics 159 (2003) 71–78, https://doi.org/10.1016/S0167-2738(03)00027-4.

[15] T. Nagai, W. Ito, T. Sakon, Relationship between cation substitution and stability of perovskite structure in SrCoO3–δ-based mixed conductors, Solid State Ionics 177 (2007) 3433–3444, https://doi.org/10.1016/j.ssi.2006.10.022.

[16] A. Aguadero, J.A. Alonso, D. Pérez-Coll, C. de la Calle, M.T. Fernández-Díaz, J. B. Goodenough, $SrCo_{0.95}Sb_{0.05}O_{3-\delta}$ as cathode material for high power density solid oxide fuel cells, Chem. Mater. 22 (2010) 789–798, https://doi.org/10.1021/cm901423g.

[17] V. Cascos, R. Martínez-Coronado, J.A. Alonso, New Nb-doped $SrCo_{1-x}Nb_xO_{3-\delta}$ perovskites performing as cathodes in solid-oxide fuel cells, Int. J. Hydrogen Energy 39 (2014) 14349–14354, https://doi.org/10.1016/j.ijhydene.2014.03.100.

[18] V. Cascos, M.T. Fernández-Díaz, J.A. Alonso, Structural and electrical characterization of the novel $SrCo_{1-x}Ti_xO_{3-\delta}$ ($x = 0.05$, 0.1 and 0.15) perovskites: evaluation as cathode materials in solid oxide fuel cells, Renew. Energy 133 (2019) 205–215, https://doi.org/10.1016/j.renene.2018.09.073.

[19] V. Cascos, L. Troncoso, M.T. Fernández-Diaz, J.A. Alonso, $SrCo_{1-x}Ru_xO_{3-\delta}$ ($x = 0.05$, 0.1, and 0.15) perovskites as outperforming cathode material in intermediate-temperature solid oxide fuel cells, ACS Appl. Energy Mater. 1 (2018) 4505–4513, https://doi.org/10.1021/acsaem.8b00376.

[20] V. Cascos, L. Troncoso, A. Larralde, C. Álvarez-Galván, M.T. Fernandez-Díaz, J. A. Alonso, $M = Ir^{4+}, Ta^{5+}$ -doped $SrCo_{0.95}M_{0.05}O_{3-\delta}$ perovskites: promising solid-oxide fuel-cell cathodes, ACS Appl. Energy Mater. 4 (2021) 500–509, https://doi.org/10.1021/acsaem.0c02404.

[21] V. Cascos, L. Troncoso, A.L. Larralde, M.T. Fernandez-Diaz, J.A. Alonso, Performance of $SrCo_{1-x}Ir_xO_{3-\delta}$ ($x = 0.10$ and 0.15) perovskites as potential cathode materials for intermediate-temperature solid oxide fuel cells (IT-SOFC), ACS Appl. Energy Mater. 3 (2020) 6709–6716, https://doi.org/10.1021/acsaem.0c00848.

[22] Y. Takeda, R. Kanno, T. Takada, O. Yamamoto, M. Takano, Y. Bando, Phase relation and oxygen-non-stoichiometry of Perovskite-like Compound $SrCoO_x$ ($2.29 < x > 2.80$), Z. Anorg. Allg. Chem. 540 (1986) 259–270, https://doi.org/10.1002/zaac.19865400929.

[23] Z.Q. Deng, W.S. Yang, W. Liu, C.S. Chen, Relationship between transport properties and phase transformations in mixed-conducting oxides, J. Solid State Chem. 179 (2006) 362–369, https://doi.org/10.1016/j.jssc.2005.10.027.

[24] F. Sears Varley, Neutron scattering lengths and cross sectioirn, Neutron News 3 (1992) 29–37.

[25] R.A. Young, The Rietveld Method, International Union of Crystallograhy, Oxford University Press, [Chester, England]; Oxford; New York, 1993.

[26] J. Rodríguez-Carvajal, Introduction to the Program FULLPROF: Refinement of Crystal and Magnetic Structures from Powder and Single Crystal Data, n.d..

[27] R. Martínez-Coronado, J.A. Alonso, A. Aguadero, M.T. Fernández-Díaz, Optimized energy conversion efficiency in solid-oxide fuel cells implementing $SrMo_{1-x}Fe_xO_{3-\delta}$, J. Power Sources 208 (2012) 153–158, https://doi.org/10.1016/j.jpowsour.2012.02.002.

[28] Z. Shijie, L. Na, S. Liping, L. Qiang, H. Lihua, Z. Hui, A novel high-entropy cathode with the A2BO4-type structure for solid oxide fuel cells, J. Alloys Compd. 895 (2022) 162548, https://doi.org/10.1016/j.jallcom.2021.162548.

[29] Q. Yang, G. Wang, H. Wu, B.A. Beshiwork, D. Tian, S. Zhu, Y. Yang, X. Lu, Y. Ding, Y. Ling, Y. Chen, B. Lin, A high-entropy perovskite cathode for solid oxide fuel cells, J. Alloys Compd. 872 (2021) 159633, https://doi.org/10.1016/j.jallcom.2021.159633.

[30] J.W. Stevenson, K. Hasinska, N.L. Canfield, T.R. Armstrong, Influence of cobalt and iron additions on the electrical and thermal properties of $(La,Sr)(Ga,Mg)O_{3-\delta}$, J. Electrochem. Soc. 147 (2000) 3213, https://doi.org/10.1149/1.1393885.

[31] M. Chivite Lacaba, A. Alveal, J. Prado-Gonjal, J.A. Alonso, M.T. Fernández Díaz, L. Troncoso, V. Cascos, Reducing the cobalt content in $SrCo_{0.95}Ti_{0.05}O_{3-\delta}$ -based perovskites to produce cleaner cathodes for IT-SOFCs, ACS Appl. Energy Mater. 6 (2023) 1046–1055, https://doi.org/10.1021/acsaem.2c03569.

[32] V. Cascos, L. Troncoso, J.A. Alonso, New families of M^{n+}-doped $SrCo_{1-x}M_xO_{3-\delta}$ perovskites performing as cathodes in solid-oxide fuel cells, Int. J. Hydrogen Energy 40 (2015) 11333–11341, https://doi.org/10.1016/j.ijhydene.2015.03.134.

[33] V. Cascos, J. Alonso, M. Fernández-Díaz, Nb^{5+}-Doped $SrCoO_{3-\delta}$ perovskites as potential cathodes for solid-oxide fuel cells, Materials 9 (2016) 579, https://doi.org/10.3390/ma9070579.